chemosensors

MDPI

Article

Effect of Ti_2CT_x MXene Oxidation on Its Gas-Sensitive Properties

Artem S. Mokrushin [1,*], Ilya A. Nagornov [1], Philipp Yu. Gorobtsov [1], Aleksey A. Averin [2], Tatiana L. Simonenko [1], Nikolay P. Simonenko [1], Elizaveta P. Simonenko [1] and Nikolay T. Kuznetsov [1]

[1] Kurnakov Institute of General and Inorganic Chemistry, Russian Academy of Sciences, 31 Leninsky pr., 119991 Moscow, Russia
[2] Frumkin Institute of Physical Chemistry and Electrochemistry, Russian Academy of Sciences, 31 Leninsky pr., bldg. 4, 199071 Moscow, Russia
* Correspondence: artyom.nano@gmail.com

Abstract: The oxidation process was studied for the synthesized low-layer Ti_2CT_x MXene deposited on a special Al_2O_3/Pt sensor substrate using in situ Raman spectroscopy. It is noted that on the ceramic parts of the substrate (Al_2O_3), the beginning of oxidation (appearance of anatase mod phase) is observed already at 316 °C, in comparison with platinum, for which the appearance of anatase is noted only at 372 °C. At the temperature 447 °C, the initial MXene film is completely oxidized to TiO_2. Using scanning electron microscopy and atomic force microscopy, the microstructure and dispersity of the obtained MXene film were studied. It was found that the obtained films exhibit chemoresistive responses to the detection of a wide group of gases, H_2, CO, NH_3, C_6H_6, C_3H_6O, CH_4, C_2H_5OH and O_2, at room temperature and RH = 50%. The highest sensitivity is observed for NH_3. The partial oxidation of the Ti_2CT_x MXene was shown to favorably affect the gas-sensitive properties.

Keywords: chemoresistive gas sensors; MXenes; T_2C; Titanium dioxide (TiO_2); Raman; 2D-nanomaterials

Citation: Mokrushin, A.S.; Nagornov, I.A.; Gorobtsov, P.Y.; Averin, A.A.; Simonenko, T.L.; Simonenko, N.P.; Simonenko, E.P.; Kuznetsov, N.T. Effect of Ti_2CT_x MXene Oxidation on Its Gas-Sensitive Properties. *Chemosensors* **2023**, *11*, 13. https://doi.org/10.3390/chemosensors11010013

Academic Editors: Kai Xu and Zhong Li

Received: 30 November 2022
Revised: 19 December 2022
Accepted: 20 December 2022
Published: 22 December 2022

1. Introduction

Two-dimensional titanium-containing carbide MXenes with the general formula $Ti_{n+1}C_nT_x$ have attracted increased attention from the scientific community in recent years due to their unique properties—a large surface-to-volume ratio, high electrical conductivity, which can be metallic or semiconducting, and surface functionalization by various groups (primarily −F, −OH, −O), whose composition can be adjusted in some limits by choice of synthesis method. [1–3]. This combination of unique MXene properties opens up the potential for their use in various fields: in lithium/sodium-ion batteries and supercapacitors [4,5], fuel cells [6,7], photocalysis [8,9], as well as chemical gas sensing [10–14] etc.

In contrast to metal oxide semiconductors (MOS), the classical receptor materials for chemoresistive gas sensors, $Ti_{n+1}C_nT_x$ MXenes often have metallic conductivity, their outer surface is completely covered by functional groups, and their morphology refers to 2D-nanomaterials. This combination makes this class of compounds attractive for chemoresistive gas sensors with a high signal-to-noise ratio (SNR) [15], including room temperature operation.

The detection of the MXenes mechanism differs significantly from MOS materials. A universal model describing the interaction of the analyte gas with ion-adsorbed oxygen and the formation of an electron-depleted layer (EDL) on the surface layer of the sensitive material can be used for MOS-gas sensors [16]. At present, the question about the mechanism of gas detection by MXenes is debatable. Nevertheless, theoretical and experimental models allowing the description of the appearance of the chemoresistive signal in the atmosphere of different gases have already been observed [17–19].

MXenes, due to their predisposition to form hydrogen bonds with functional groups, are extremely sensitive to moisture. The harmonic structure characteristic of MXenes

multilayer, the metallic type of conductivity, and the fact that water molecules do not form covalent bonds with the surface of MXenes make them extremely sensitive to humidity and allow a reproducible response. In Zhang C. et al. [20], using FT-IR spectroscopy and the study of the wetting angle on the MXenes surface, the authors found that water molecules from the gas phase can be chemically sorbed on the surface and in the interlayer space of $Ti_3C_2T_x$ MXene. The authors proposed a mechanism whereby the hydroxyl groups thus formed on the surface provide an electrostatic field and prevent charge transfer, which is explained by an increase in electrical resistance (positive response: *p*-type) with increasing humidity. The nanoscale interlayer space (~1.01 nm) of $Ti_3C_2T_x$, as well as the surface super hydrophilicity found by the authors, prevents capillary condensation of water and limits the movement of hydroxyl groups, which are characteristic of bulk nanomaterials.

Structural water plays an important role in reducing the overall interaction between the MXenes layers and creating additional space for the adsorption and diffusion of gases with affinity to functional groups. This feature is an advantage over other 2D-layered materials, such as graphene, in which strong Van-der-Waals interactions between two-dimensional sheets and small interlayer distances prevent the intercalation of gas molecules. Koh H-J. et al., in their article [21], in situ using XRD demonstrated that the interlayer space of MXenes contains water fragments (hydroxyl groups or water molecules themselves), which can be removed when the material is exposed to dry nitrogen. The authors showed that ethanol molecules can chemically bind with $Ti_3C_2T_x$ MXene in its interlayer space. As a result of these interactions, the MXene swells, and its interlayer distance increases due to the steric effect. The swollen two-dimensional MXene decreases the number of electrons involved in charge transfer between the layers during ethanol detection, which leads to an increase in electrical resistance and allows the positive (*p*-type) chemoresistance response to be recorded.

The MXenes show the best sensitivity when detecting gases able to form hydrogen bonds. Majhi S.M. et al., in article [18], showed a positive (*p*-type) response when acetone is detected by the $Ti_3C_2T_x$ MXene. Kim S.J. et al. [15] also showed that when used as a receptor material, $Ti_3C_2T_x$ MXene demonstrates the greatest response to gases capable of forming a hydrogen bond (acetone, ethanol, propanal and ammonia) than observed for acid gases (NO_2, SO_2 and CO_2). The authors demonstrated the ability to detect 50–1000 ppb of acetone, ethanol and ammonia with a low SNR value. DFT calculations found that hydroxyl groups (−OH) made the largest contribution to acetone bonding to functional groups on the $Ti_3C_2T_x$ MXene surface compared to oxygen (−O) and fluoride (−F) groups. It was found that for OH-groups, the bonding energy value is significantly more negative compared to −O and −F: −0.774 compared to −0.317 and −0.311 eV, respectively. The authors concluded that the terminal hydroxyl groups on the surface of MXenes play a key role in the detection of various gases to form hydrogen bonds [15].

In most of the papers presented in the literature, a positive chemoresistive response of the *p*-type is recorded when detecting various gases with carbide titanium-containing MXenes. Nevertheless, there are also studies in which the electrical resistance decreases when gases are injected (negative response: *n*-type). For example, Wu M. et al. [22] observed a decrease in electrical resistance when detecting ammonia by the $Ti_3C_2T_x$ MXenes. The authors explain this by the strong functionalization of the surface by chloride groups (−Cl), which were formed on the surface of MXenes due to the peculiarities of the synthesis (etching MAX-phase in the Lewis acid $ZnCl_2$ melt, which is different from the classical liquid-phase methods). This phenomenon is not fully explained in this paper. The authors suggest that chloride groups can affect the MXene band structure, which leads to the reverse chemoresistive response.

Nanocomposites based on them, primarily based on titanium dioxide $Ti_{n+1}C_nT_x/TiO_2$, are no less interesting receptor materials for gas sensors as compared to individual $Ti_{n+1}C_nT_x$ MXenes. Such nanocomposites can be obtained, in particular, by thermal oxidation in an oxygen-containing atmosphere of the initial $Ti_{n+1}C_nT_x$ MXenes. Such $Ti_{n+1}C_nT_x/TiO_2$ nanocomposites can have improved gas-sensitive characteristics. In [23], the authors oxi-

dized a $Ti_3C_2T_x$ film deposited on a special multi-sensor chip in air at 350°C. The resulting nanocomposite demonstrated an increased semiconductor response to ethanol at relatively high temperatures (300–350 °C), and a decrease in the response and recovery time of the sensor was noted. In [24], the authors used oxygen plasma to oxidize MXene. The resulting nanocomposite showed an increased response to ethanol by several orders of magnitude. The formation of $Ti_{n+1}C_nT_x/TiO_2$ nanocomposites is also possible by holding MXene in an aqueous solution, specifically under the influence of light. In [25], the authors obtained $Ti_{n+1}C_nT_x/TiO_2$ by holding the individual components in an ethanol-water mixture. For the synthesized nanocomposite, they were able to increase the sensitivity, as well as lower the threshold of sensitivity to ammonia to 100 ppb. In [26], the authors in situ-oxidized the initial $Ti_3C_2T_x$ MXene using hydrothermal synthesis. The resulting oxidized nanocomposite demonstrated increased sensitivity and selectivity to NO_2 detection. In [27], the authors used a "simple spray method" to spray an aqueous dispersion of TiO_2 onto the surface of $Ti_3C_2T_x$ MXene. The resulting nanocomposite showed improved gas-sensitive characteristics when detecting low NH_3 concentrations at RT, as well as a more stable signal compared to the individual $Ti_3C_2T_x$ MXene.

The present paper is devoted to the study of the oxidation process of the $Ti_3C_2T_x$ MXene film using in situ Raman spectroscopy and to the study of the gas-sensitive chemoresistance properties of the obtained nanomaterials to a wide group of analyte gases.

2. Materials and Methods

2.1. Mxene Synthesis and Film Application

Reagents: powders of metallic titanium (99.9%, 0.5–100 μm, Ruskhim, Moscow, Russia), aluminum (99.2%, 30 μm, Ruskhim), graphite (MPG-8 grade, Ruskhim), potassium bromide KBr (99%, Ruskhim), sodium fluoride NaF (osc. Part 9-2, Reackhim, Moscow, Russia), hydrochloric acid HCl (>99%, Sigma Tech, Moscow, Russia), tetramethylammonium hydroxide solution $(CH_3)_4N(OH)$ (TMAOH, 25%, aqueous solution, Technic, Saint-Denis, France).

The synthesis of Ti_2CT_x MXene was performed by selective etching of aluminum layers contained in the MAX-phase of Ti_2AlC. For this purpose, Ti_2AlC powder was added to a sodium fluoride solution in hydrochloric acid; the Ti_2AlC and Ti_2CT_x synthesis techniques used in this study are described in detail in [28,29].

Briefly, to obtain Ti_2AlC, powders of aluminum, titanium, graphite and potassium bromide were mixed in the ratio n(Ti):n(Al):n(C) = 2:1.2:0.8 and m(Ti+Al+C) = m(KBr), then co-milled, pressed into tablets and heat treated in a muffle furnace at 1000 °C in a protective melt KBr.

To obtain the multilayer Ti_2CT_x MXene, a 1 g sample of the MAX-phase Ti_2AlC mass was slowly added to 20 mL of 6 M HCL solution with 1 g of NaF. The system was then incubated under stirring and at 40 ± 5 °C for 24 h. The resulting powder was separated by centrifugation and repeatedly washed with distilled water until pH ~5–6 was reached. Delamination was performed using tetramethylammonium hydroxide $(CH_3)_4N(OH)$ solution under ultrasonic influence.

The obtained Ti_2CT_x MXene sample was held in an aqueous dispersion at 4–6 °C for 7 days and then used to apply the receptor layer.

The Ti_2CT_x MXene film was deposited by drop casting method on the surface of a specialized Al_2O_3 substrate with platinum interdigital electrodes (from the front side) and a platinum microheater (from the back side). For this purpose, the dispersion system (carbide nanosheets and deionized water in a volume of 50 μL) was applied to the substrate surface in the area of counter-pin electrodes using an automatic dispenser. Then, a step drying in the range of 25–150 °C under reduced pressure was performed to remove the solvent.

2.2. Instrumentation

The microstructure and chemical composition of the film surface were studied by scanning (NVision 40 scanning electron microscope, Carl Zeiss (Oberkochen, Germany,

secondary electron detector, accelerating voltage 1–10 kV) and transmission electron microscope (JEOL JEM-1011, Akishima, Japan), as well as X-ray spectral elemental microanalysis (energy-dispersive X-ray (EDX) spectrometer INCA X-MAX 80, Oxford Instruments (Oxford, UK), accelerating voltage 20 kV). The powder phase composition and films were studied by means of X-ray diffraction (XRD) on D8 Advance device (Bruker, Billerica, MA, USA,), CuKα = 1.5418 Å, Ni filter, E = 40 keV, I = 40 mA; the range of 2θ: 5–45°; resolution: 0.02°; signal accumulation time in the point: 0.3 s).

The obtained Ti_2CT_x MXene films were examined by atomic force microscopy (AFM). Surface topography and Kelvin-probe force microscopy (KFM) were studied on a Solver Pro-M scanning probe microscope (NT-MDT production, Zelenograd, Moscow, Russia) using ETALON HA-HR probes with W_2C-based conductive coating (tip curvature <35 nm). The microstructure of the obtained films was studied using SEM and AFM on the Al_2O_3 section between platinum microelectrodes.

Raman spectra were obtained with a Renishaw inVia Reflex Microscope system equipped with a Peltier-cooled CCD. The 532-nm lines of a Nd:YAG laser were used for excitation. The laser light was focused on the sample through a 50× objective to a spot size of ~2 μm. The power of the sample was <0.3 mW. The variable-temperature Raman scattering measurements were made using a THMS600 stage (Linkam Scientific Instruments Ltd., Redhill, UK). The in situ film heating rate was 5 °C/min. After conducting Raman in situ heating experiments on the samples, the temperature was recalibrated on a typical sample using a high-precision Testo 868 thermal imaging camera. Due to the fact that Raman spectroscopy can be destructive for some samples (especially those prone to oxidation, as in this case) due to local heating of the region from which the spectrum is taken after laser exposure, spectra were recorded in different areas of the film, which are nevertheless localized close to each other. This approach avoided the local overheating that could occur with repeated laser exposure, even at low power, which allowed more reliable data to be obtained. All spectra obtained were normalized with respect to the most intense spectrum.

The chemoresistive responses were obtained using a special laboratory setup, a detailed description of which can be found in our earlier papers [30,31]. The gas medium was created in a quartz cell using two Bronkhorst gas flow controllers with a maximum throughput of 100 and 200 mL/min. The quartz cell volume is 7×10^{-5} m^3. The electrical resistance of the obtained oxide films was measured using a Fluke 8846A Digit Precision Multimeter, which has an upper detection limit of 1000 MΩ. The temperature of the sensor was monitored using a platinum microheater pre-calibrated with a high-precision Testo 868 thermal imaging camera. The measurements of gas-sensitive properties, among others, were carried out at room temperature. Before starting the gas-sensitive measurements, the film to be measured was incubated in a baseline gas atmosphere until a stable signal was established.

To measure the signal at different relative humidity (RH), we used a special unit with a bubbler flask; the RH of the gas mixture was controlled by a digital flow-through hygrometer "Excis". The temperature value of the relative humidity was set and then measured at 20 °C.

All gas-sensing measurements were carried out at room temperature (RT) and 50% relative humidity. The response to H_2, CO, NH_3, benzene (C_6H_6), acetone (C_3H_6O), methane (CH_4), ethanol (C_2H_5OH) and oxygen (O_2) was calculated using the following ratio:

$$S_1 = \frac{|R_{BL} - R_g|}{R_{BL}} \times 100\% \quad (1)$$

where R_{BL} is the baseline resistance (nitrogen (99.9999%) and was used as the baseline for oxygen detection and synthetic air for other gases, and R_g is the resistance at a given concentration of analyte gas.

The response to humidity was calculated using the following ratio:

$$S_2 = \frac{|R_{BL} - R_{RH}|}{R_{BL}} \times 100\% \quad (2)$$

where R_{BL} is the resistance at 30% relative humidity, and R_{RH} is a given relative humidity.

3. Results and Discussion

3.1. Investigation of the Phase Composition and Microstructure of the Obtained Ti_2CT_x Mxene

As shown in Figure 1a, the obtained MXene sample contains no significant admixtures of the original Ti_2AlC, and the shift in the reflex position (002) toward lower angles to $2\theta = 4.6^\circ$ indicates the successful delamination of the multilayer aggregates formed by etching the MAX-phase with NaF-HCl. The shift of the reflex associated with the Ti_2CT_x phase for the coating on the specialized substrate toward higher angles to $2\theta = 5.3^\circ$ indicates that the reverse aggregation of the MXene sheets and the decrease in the interlayer distance during vacuum drying occurs during coating formation.

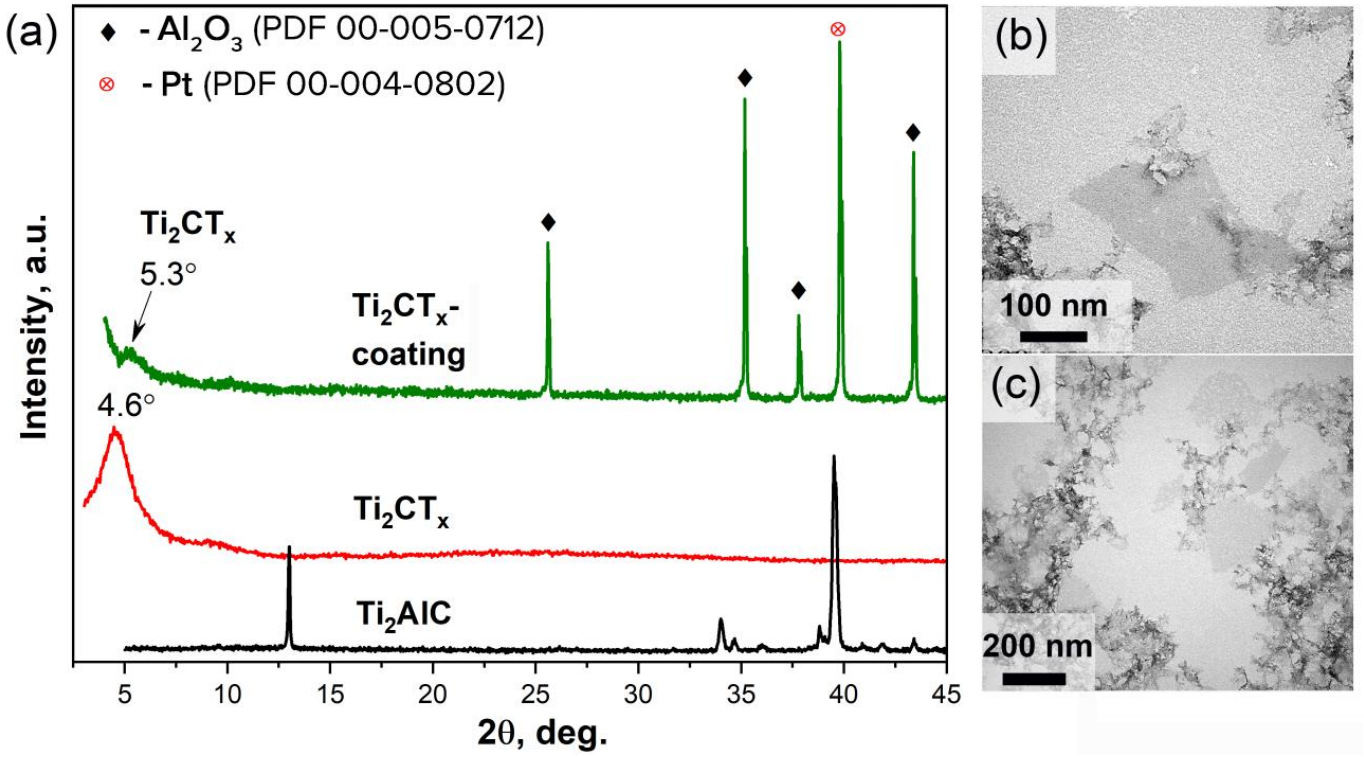

Figure 1. The X-ray patterns of the initial Ti_2AlC, low-layer Ti_2CT_x MXene and its coating on a specialized sensor substrate (**a**), and TEM microphotographs of Ti_2CT_x MXene (**b**,**c**).

The TEM data indicate partial destruction of the MXene sheets (Figure 1b,c) while holding it in aqueous dispersion, as well as the appearance of loose nanoparticles on the sheet boundaries, probably related to oxidation products—titanium dioxide in different crystalline modification.

3.2. Raman Spectroscopy

In situ Raman spectra recording for Ti_2CT_x MXene films on an Al_2O_3 chip with Pt interdigital microelectrodes (Figure 2a) was performed both for platinum microelectrodes and for the Al_2O_3 area between them (Figure 2b). The results of which can be attributed to the inhomogeneity of the prepared film. It should be noted that modes on the Raman spectra characteristic of the MXene phase are more intensive on platinum.

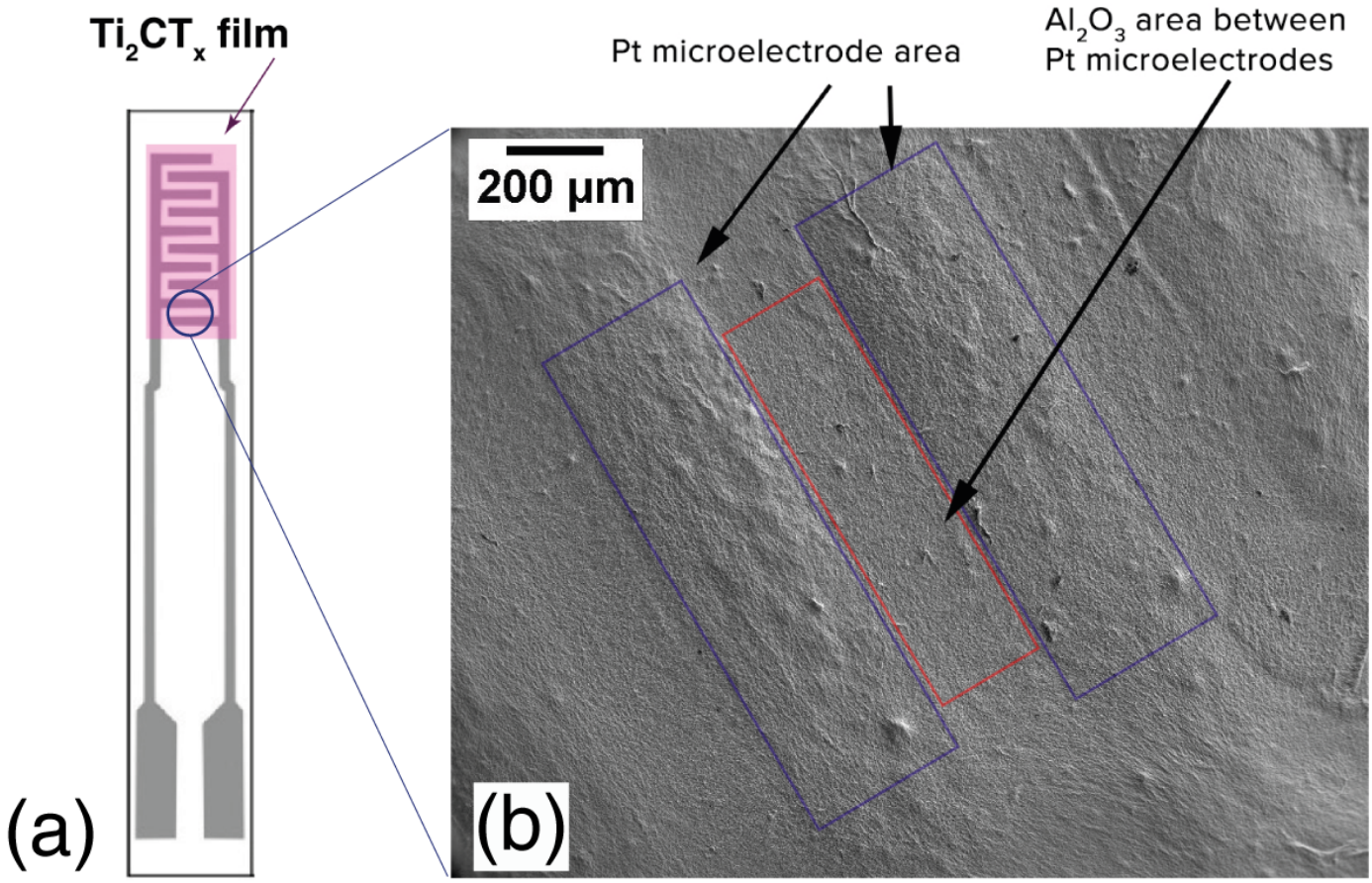

Figure 2. The scheme of an Al_2O_3 substrate with Pt microelectrodes and Ti_2CT_x MXene film (**a**) and a microphotograph of the Ti_2CT_x film on the substrate surface with an indication of the areas where in situ Raman spectra were measured (**b**).

3.2.1. MXene Raman Spectra for the Platinum Electrodes Area

A Ti_2CT_x MXene film is characterized by three normal modes, ω_1, ω_2 and ω_3, in Raman spectra, located at 270, 380 and 697 cm^{-1}, respectively (Figure 3a). Modes ω_1-ω_3 can be attributed both to vibrations of MAX-phase Ti_2AlC, remaining after synthesis, and to Ti_2CT_x MXene itself [32–35]. Analysis of the spectrum obtained at RT also reveals other modes: ω_{R1} and ω_{R2} modes are located at 447 and 821 cm^{-1}, which can be attributed to high convergence to E_g and B_{2g} modes characteristic of rutile TiO_2 [36,37]. For the rutile phase, the largest intensity should be observed for E_g and A_{1g} modes with maxima at ~448 and 613 cm^{-1}, respectively, while B_{2g} should be the least intensive of all first-order modes characteristic of rutile [38]. In this case, however, the ω_{R2} (B_{2g}) mode is the most intensive of all rutile phase modes, which is highly irregular for rutile TiO_2 materials in the literature [38,39]. Such behavior allows us to suppose that the obtained MXene at RT does not include a separate rutile TiO_2 phase, with observed ω_{R1} (E_g) and ω_{R2} (B_{2g}) modes arising from Ti−O bonds, with energies close to analogous bonds in rutile, on the MXene surface. Moreover, the observed rutile species on the surface of Ti_2CT_x MXene likely formed as a result of keeping the synthesized sample in water suspension.

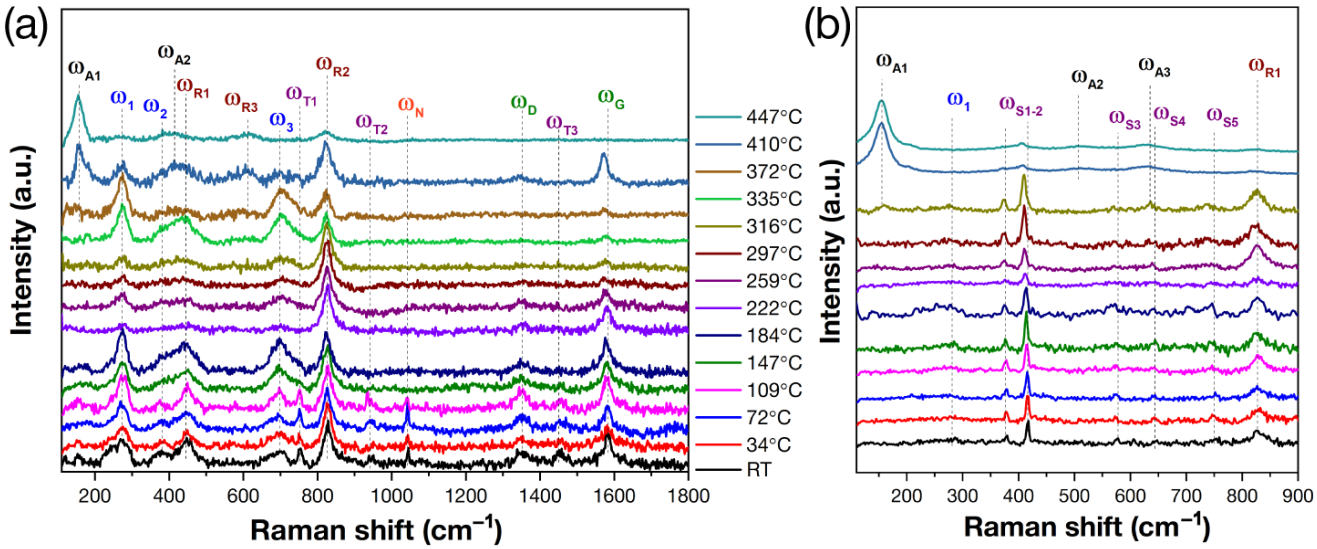

Figure 3. In situ Raman spectra at different temperatures (20–447 °C) of the thin film at different substrate areas: on Pt (**a**) and Al_2O_3 (**b**).

In the more long-wave region of the spectrum, ω_D and ω_G modes are located at 1349 and 1583 cm^{-1}, which are characteristic carbon D- and G-bands [32], which are common for many carbon systems with sp^2 hybridization of the C−C bond. Therefore, they can be attributed to carbon in MXene as well as to graphene layers resulting from the excessive etching of Ti_2AlC by hydrofluoric acid and the partial removal of titanium atoms beside aluminum atoms [40–42].

In addition to the main MXene modes, low-intensity modes ω_{T1}, ω_{T2} and ω_{T3} were found at 754, 935 and 1454 cm^{-1}, respectively. Modes ω_{T1}-ω_{T3} are characteristic of tetramethylammonium hydroxide (TMAOH) [43], fragments of which had likely been captured in MXene interlayer space after delamination and washing. At 1042 cm^{-1}, the ω_N mode is also present, attributed to the nitro group (NO_3^-) [44,45], which could have formed on the MXene surface after the gas-sensing properties studies in an atmosphere containing NO_2. The possibility of gaseous NO_2 transformation into an NO_3- group on the surface of the $Ti_3C_2T_x/TiO_2$ material has been considered in studies [46,47].

The described set of modes is retained by the sample under heating up to 109 °C. At higher temperatures, the spectra undergo significant changes. Starting with 147 °C, no ω_{T1}-ω_{T3} and ω_N modes (characteristic of TMAOH and NO_3^- groups, respectively) appear in the spectra. This can be attributed to their desorption and/or decomposition with the following desorption of gaseous decomposition products from the MXene surface. Heating to ≥147 °C results in the overlap of ω_2 mode with the rutile ω_{R1} band, yielding a new widened peak. Further heating leads to the transformation of this peak with maximum shifting to a lower wave number. At 410 °C, the maximum of this phase is located at 420 cm^{-1}, which is close to the B_{1g} mode of the titanium dioxide anatase phase [38]. This might indicate partial restructuring of the crystal lattice. Modes characteristic of Ti_2CT_x (ω_1 and ω_3), as well as of TiO_2 rutile (ω_{R2}), still remain on the film spectra, with their maxima not undergoing any changes.

The most intensive E_g mode at 156 cm^{-1} (ω_{A1}), characteristic of anatase, starts to appear on spectra at 372 °C. The intensity of this mode rises with the temperature, which indicates that MXene is being oxidized to titanium dioxide. The A_{1g} mode at 608 cm^{-1} (ω_{R3}), which is the most intensive mode of the rutile phase [38], also appears on the Raman spectra at temperatures ≥ 372 °C as a result of the oxidation process. The Raman spectrum at 447 °C significantly differs from those recorded for the MXene film at lower temperatures, having the following set of bands: ω_{A1} (E_g) and ω_{A2} (B_{1g}) at 156 and 396 cm^{-1} from the

anatase phase and ω_{R3} (A_{1g}) and ω_{R2} (B_{2g}) at 615 and 821 cm^{-1} from the rutile phase. The obtained values are in good agreement with the literature [37,38].

D- and G-modes are retained up to the temperature of 447 °C. An increase in temperature gives rise to the systematic shift of the G-mode to lower wave numbers. Thus, at 410 °C, the G-mode maximum is situated at 1570 cm^{-1}. The shift of the maximum position can be related to temperature effects arising from in situ heating of the sample.

Thus, analysis of the recorded Raman spectra for MXene film on platinum allows us to infer that the oxidation of MXene begins at 372 °C. It is at this temperature that the Ti_2CT_x/TiO_2 composite with a large content of rutile and anatase phases of TiO_2 forms. At the temperature of 447 °C, the Ti_2CT_x/TiO_2 film fully oxidizes TiO_2, consisting of rutile and anatase.

3.2.2. Raman Spectra for the Al_2O_3 Area

Considering the features of sensing studies, it is the Raman spectra of MXene on a ceramic Al_2O_3 surface between platinum microelectrodes that are of the most interest since chemoresistive signals of the gas-sensitive film arise from this area of the sample. We have observed that Ti_2CT_x spectra recorded on local areas on the Al_2O_3 surface significantly differ from those recorded for MXene film areas situated on the surface of platinum electrodes. We were able to obtain intensive signals for Ti_2CT_x on the surface of the platinum electrodes related to vibrations of various phases. On the Al_2O_3 surface, however, most modes are of low intensity, and for the initial TI_2CT_x spectrum, large background luminescence was observed, which obstructs registering Raman scattering. For this reason, only the region up to 900 cm^{-1} is shown in the graph with characteristic MXene modes and oxidation products.

On all spectra of the MXene film (Figure 3b), the characteristic set of modes ω_{S1}-ω_{S5}, typical for α-Al_2O_3 substrate, can be seen at 377, 417, 574, 644 and 749 cm^{-1} [48]. At RT, only weak ω_1 mode of MXene at 276 cm^{-1} and intense mode ω_{R2} (B_{2g}) at 828 cm^{-1} from rutile (these modes were the most intense for Raman spectra of MXene on the platinum surface—see Section 3.2.1) are observed. No other modes, characteristic of MXene, were found for the film on Al_2O_3's surface due to their low intensity and background luminescence. The described set of modes is retained up to 316 °C when the E_g (1) mode at 156 cm^{-1} (ω_{A1}) from anatase, as well as E_g (3) at 634 cm^{-1} (ω_{A3}), appear, with the latter mode not observed in spectra for the platinum surface. The obtained data are in good agreement with those in the literature [38]. It should be noted that the start of anatase formation owing to MXene oxidation already starts at 316 °C on the Al_2O_3 substrate, while for the platinum substrate, the same is only observed at 372 °C. Further increases in temperature to 410–447 °C result in full oxidation of MXene to TiO_2. Modes characteristic of anatase can be observed in this case on the Raman spectra: strong E_g (1) at 156 cm^{-1} (ω_{A1}) and weaker B_{1g}(2) + A_{1g} at 510 (ω_{A2}) and E_g(3) at 634 cm^{-1} (ω_{A3}), as well as B_{2g} at 828 cm^{-1} (ω_{R2}) from the rutile phase [38]. It should be noted that on Al_2O_3's surface, the oxidation of Ti_2CT_x MXene can be seen to proceed with the formation of mostly anatase phase. Only the weak B_{2g} mode can be attributed to rutile, which was present from the start. In the case of the final Raman spectra for platinum substrate, ω_{R1} (E_g) and ω_{R3} (A_{1g}) of the rutile phase can be observed. These seeming differences in oxidation behavior of the Ti_2CT_x MXene-receptive layer can be connected to the effect of the substrate material used for MXene film deposition on the recorded Raman spectra.

For further studies of the gas-sensing properties of the prepared Ti_2CT_x/TiO_2 nanocomposite, we have chosen the film oxidized at the minimal temperature of 316 °C.

3.3. Microstructure

SEM micrographs for films on the special Al_2O_3/Pt substrate are given in Figure 4. The initial MXene film (Figure 4a,b) exhibits the folded wavelike microstructure: the surface is reminiscent of sea crests. The length of such crests can reach several microns. It can be seen from the micrograph that the film surface is rather developed, which is important for

gas-sensing applications, which require a high specific surface area for better adsorption of gases from the atmosphere. Separate nanoparticles can also be seen on the micrographs, having a mostly spherical shape, with sizes of about 200 nm. Such particles might consist of impurities.

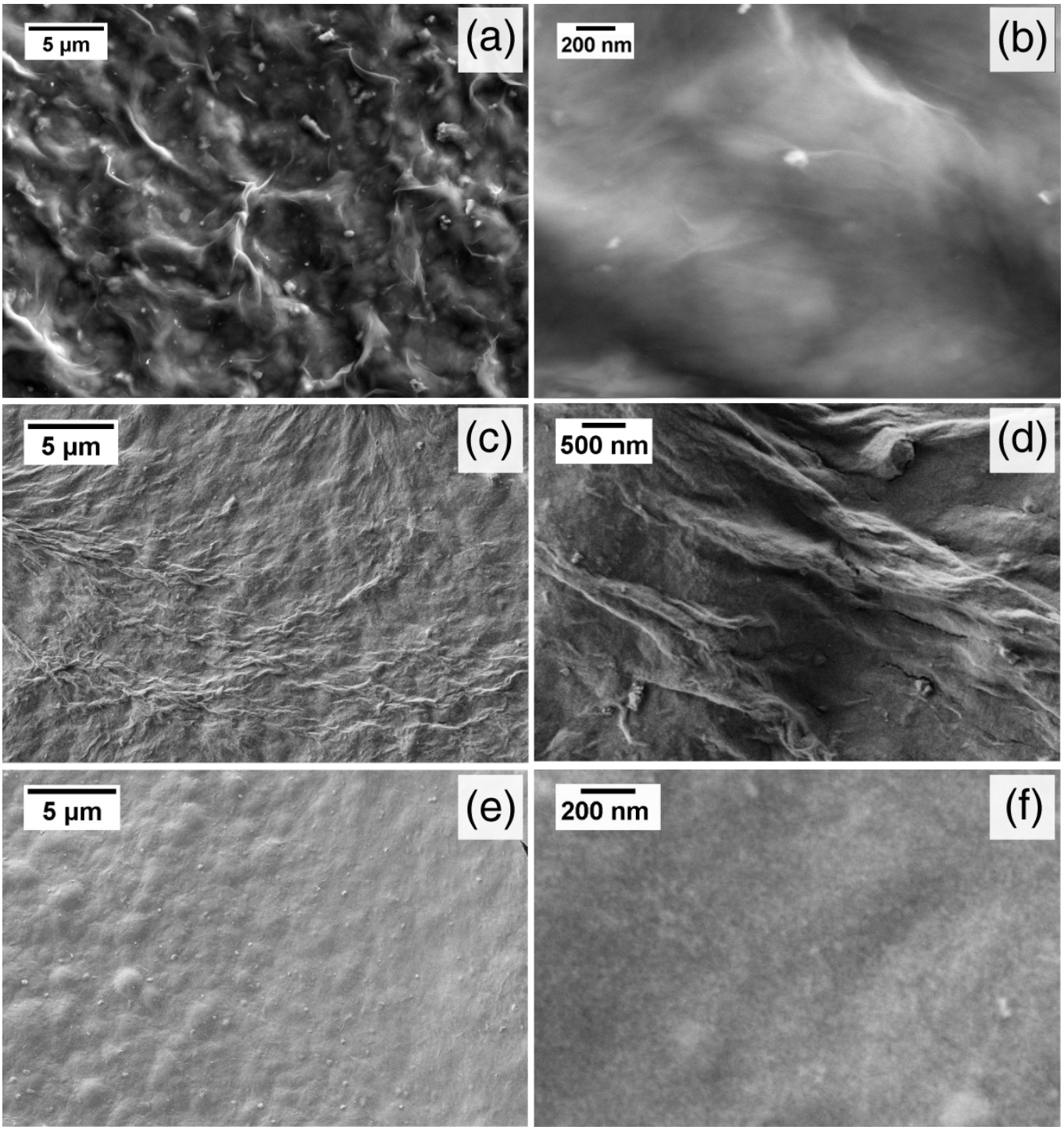

Figure 4. The SEM micrographs of films on a special Al_2O_3/Pt substrate: initial MXene (**a**,**b**), oxidized at 316 °C (**c**,**d**) and 447 °C (**e**,**f**).

Heating up to 316 °C gives rise to significant microstructural changes in the MXene film (Figure 4c,d). It becomes more uniform, although the wavelike microstructure is retained. Spherical particles 1–3 μm in diameter start to appear, most likely being aggregates of

TiO_2 in rutile crystal modification. The enlargement of TiO_2 particles can be attributed to the aggregation of smaller particles, as well as to overall phase transformation due to heat treatment of the films. Judging from Raman spectroscopy data given earlier, a nanocomposite is formed under such temperatures, consisting of the MXene phase and TiO_2.

Further increases in heat treatment temperature to 447 °C result in even more pronounced changes in the microstructure (Figure 4e,f). The wavelike structure fully gives way to a smoother surface, consisting mostly of spherical aggregates 1–3 μm in diameter. Smaller spherical nanoparticles, 20–50 nm in size, can be seen from micrographs with higher magnification (Figure 4f). Raman spectroscopy analysis suggests that under such temperatures, the TiO_2 film forms, consisting of a rutile and anatase phases mixture.

The microstructure of MXene films after their heat treatment at 316 and 447 °C was additionally studied using AFM. Topography scans are given in (Figure 5a,b), as well as the distribution of surface potential for the sample of MXene film oxidized at 316 °C. Topography results from AFM are in good agreement with SEM results (Figure 4c,d). Areas with spherical aggregates 2–4 μm in size, as well as narrow (width of ~100–250 nm) and elongated wavelike structures, roughly 100 nm in size, can be seen. Surface potential values for different film areas differ noticeably, with a work function changing varying from 4.57 to 5.00 eV, which is a consequence of film inhomogeneity. The mean work function value was 4.71 eV, which is rather close to the value for individual Ti_2CT_x MXene with a varyingly functionalized surface: 4.5–4.98 eV [49,50]. Thus, the obtained AFM results correlate well with Raman spectroscopy and SEM data and also confirm the formation of the Ti_2CT_x/TiO_2 nanocomposite.

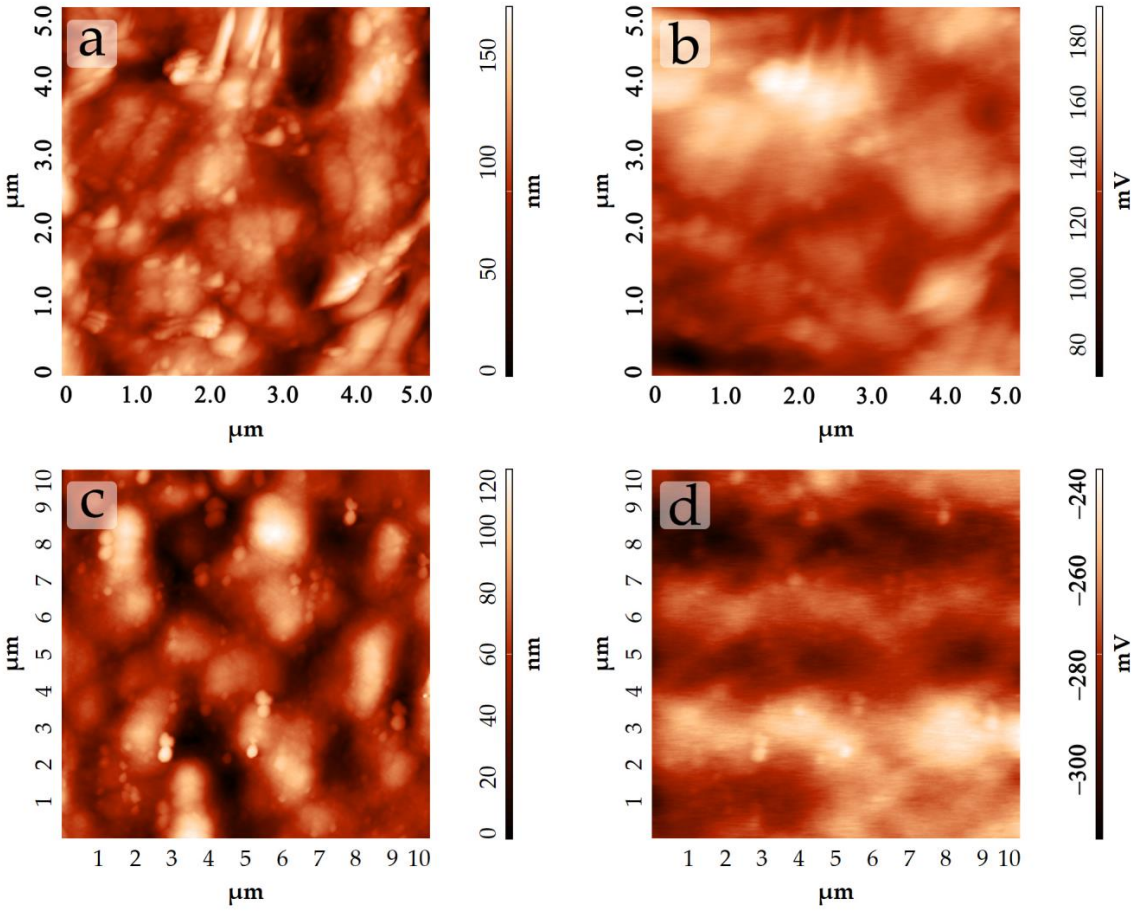

Figure 5. The AFM results: topography (**a**) and surface potential distribution map (**b**) of Ti_2CT_x/TiO_2 MXene film oxidized at 316 °C; topography (**c**) and surface potential distribution map (**d**) of Ti_2CT_x/TiO_2 film oxidized at 447 °C.

The topography scans are given in (Figure 5c,d), as well as the distribution of the surface potential for the sample of the MXene film oxidized at 447 °C. The obtained film surface is relatively smooth, consisting of low (50–80 nm) spherical aggregates 2–4 μm in size, with small spherical agglomerates 200–400 nm in size situated on their edges and in between them. Under higher magnification and in the phase contrast regime, nanoparticles with a shape close to spherical, size of ~45–95 nm, were found, which is in agreement with the SEM results. The mean square roughness on an area of 100 μm^2 is just 20 nm. It can be seen from the map of the potential surface distribution obtained from KPFM (Figure 5d) that charge carriers are spread relatively uniformly on the film surface. The mean work function value for all scanned areas was 5.00 eV. This value is in good agreement with those reported in the literature for anatase [51]. For anatase, the work function lies in the range of 4.94–5.07 eV, while for rutile, it is ~4.80 eV. Thus, AFM also confirms the formation of TiO_2 with mostly anatase crystal structure.

3.4. Gas-Sensing Chemoresistive Properties

The gas-sensitive chemoresistive properties at room temperature were studied for the initial Ti_2CT_x MXene film as well as the Ti_2CT_x/TiO_2 film oxidized in situ in a Raman spectroscopy cell at 316 °C. A further increase in the operating temperature (including in an atmosphere of high humidity) led to a significant increase in electrical resistance (R > 1 GOhm), which made it impossible to measure the gas-sensitive properties.

In the first stage, the obtained Ti_2CT_x and Ti_2CT_x/TiO_2 films had their baseline resistances measured in an atmosphere of dry air and dry nitrogen. In both cases, the resistance of the films exceeded 1 GOm, which did not allow their gas-sensitive properties to be measured in these atmospheres. The Ti_2CT_x and Ti_2CT_x/TiO_2 films showed increased chemoresistance sensitivity to humidity: a significant decrease in the baseline was observed as the RH increased. Figure 6a shows the responses to humidity variations in the air atmosphere. As can be seen, when the RH was increased from 30% to 40%, 50%, 64% and 93%, the response value increased from 0% to 46%, 67%, 83% and 96% and to 50%, 76%, 87% and 91% for Ti_2CT_x and Ti_2CT_x/TiO_2, respectively. The initial Ti_2CT_x film showed a higher sensitivity to humidity at elevated RH values (93%). The high MXenes sensitivity to humidity is typical and is well described in the literature. For further gas-sensitive measurements, a gas atmosphere with constant humidity RH = 50% was chosen.

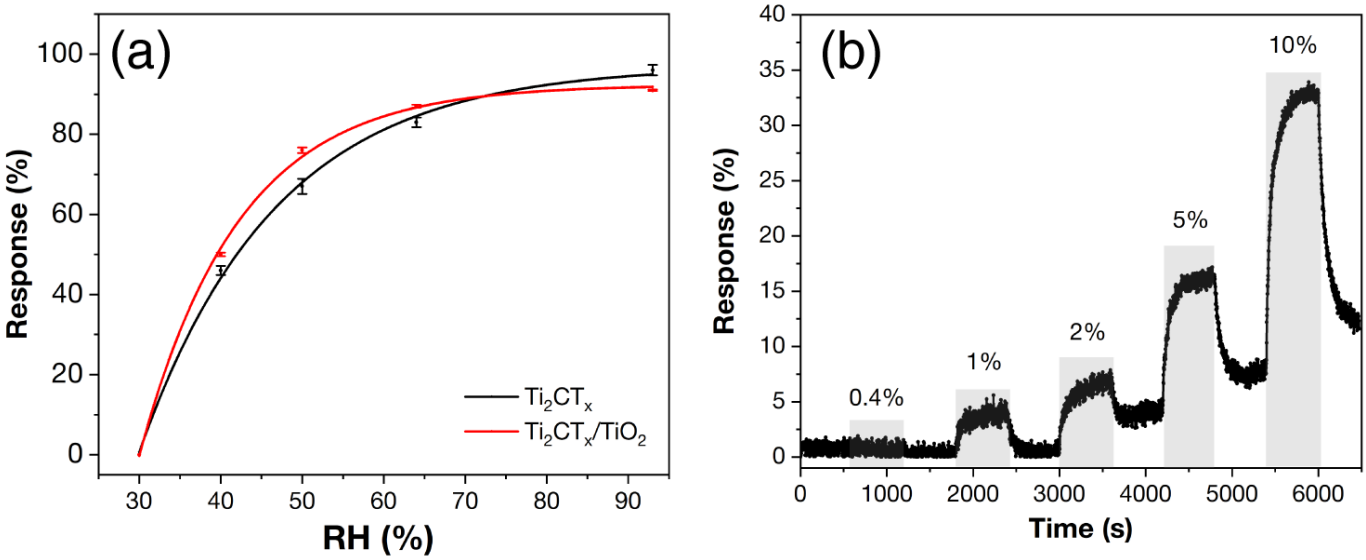

Figure 6. The responses of Ti_2CT_x and Ti_2CT_x/TiO_2 films to humidity (**a**) and Ti_2CT_x films to 0.4–10% O_2 at 50%RH (**b**).

In the following step, the chemoresistive responses were determined for the detection of 100 ppm CO, NH_3, benzene (C_6H_6), acetone (C_3H_6O), ethanol (C_2H_5OH) and 1000 ppm

methane (CH_4), H_2. The experimental responses (S1) to the above gases are shown in Figure 7a,b. The selectivity diagrams (Figure 7c,d) are plotted from the obtained response array. The bar chart (Figure 7c) shows the sign of the resulting response: a positive value corresponds to an increase in electrical resistance when the analyte gas is injected (*p*-response), and a negative value corresponds to a decrease (*n*-response). The radar chart (Figure 7d) shows the response values (S1 in %) for all analyzed gases.

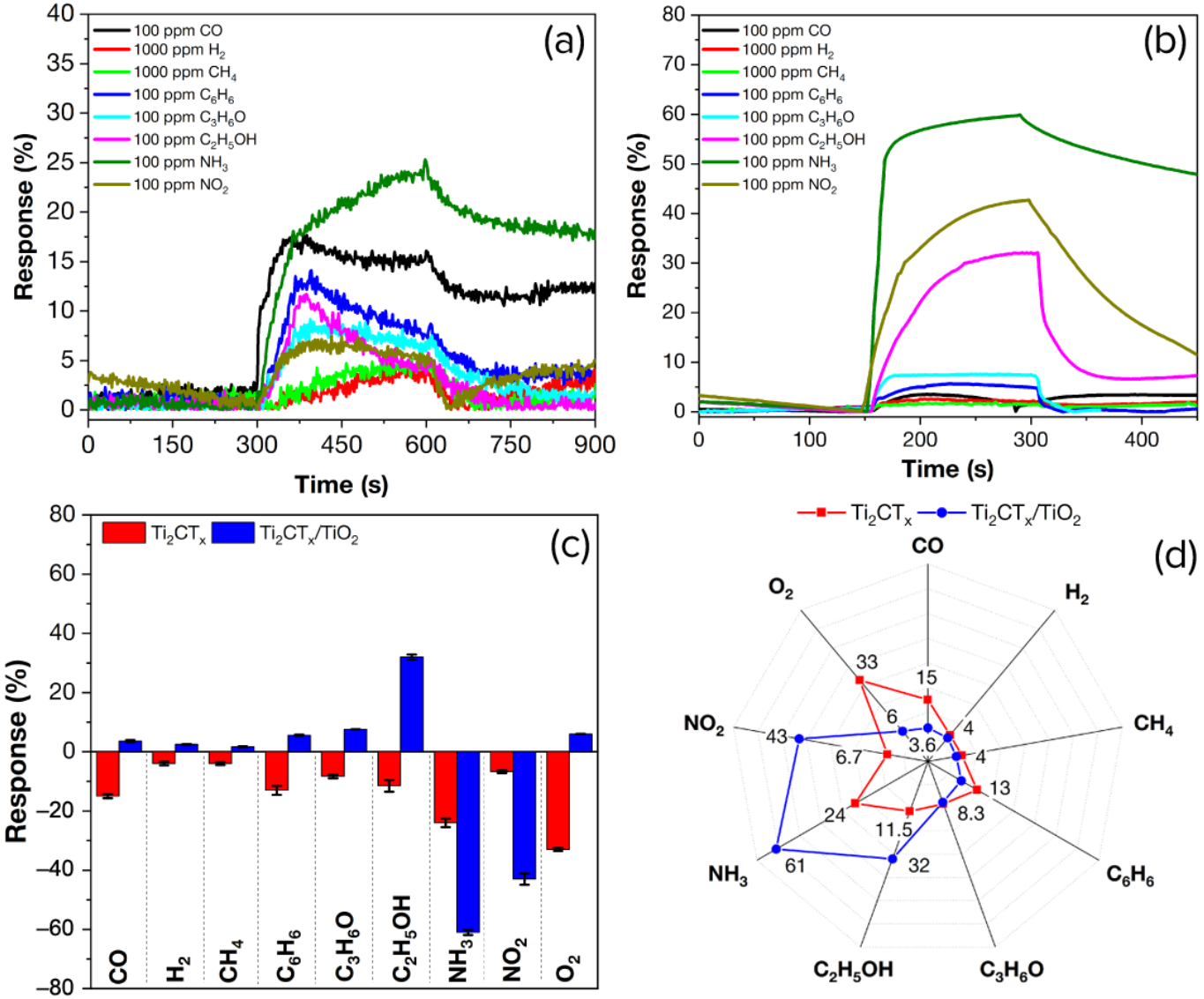

Figure 7. The gas-sensing properties of the samples at RT and 50%RH: responses to 100 and 1000 ppm of different gases of the Ti_2CT_x film (**a**) and Ti_2CT_x/TiO_2 (**b**); selectivity diagrams plotted from the responses to the different gases (**c**,**d**).

For the initial Ti_2CT_x MXene film containing its oxidation products in water dispersion, the highest response (24%) was observed when NH_3 was detected. Notable responses were recorded for CO (15%), C_6H_6 (13%), C_2H_5OH (11.5%) and C_3H_6O (8.3%); the response for H_2 and CH_4 detection was 4%. The sensitivity to 0.4–10% oxygen was also additionally measured (Figure 6b). A gradual increase in the response (S1) from 4% to 33% was observed when the oxygen concentration was increased from 1% to 10%. The response to oxygen by MXenes is practically not described in the literature but was nevertheless recorded by us in our previous study [29]. When all the above gases were injected, regardless of their chemical nature, the resistance decreased, i.e., an *n*-response was observed.

A significant change in gas-sensitive properties was observed for the Ti_2CT_x/TiO_2 composite film obtained by oxidation in air at 316 °C. The highest response (61%) was recorded for NH_3 detection, as for the initial Ti_2CT_x film. Further, notable responses were obtained for the detection of C_2H_5OH (32%) and NO_2 (43%), and the response for all other gases did not exceed 7.6%. As can be clearly seen from the selectivity radar chart (Figure 7d), the oxidized Ti_2CT_x/TiO_2 film showed an increased response to all analyzed gases (except oxygen) compared to the Ti_2CT_x film. Especially noticeable is the sensitivity to NO_2 (the response increased by 10 times), as well as a completely absent response to oxygen. In contrast to the Ti_2CT_x film, for the air-oxidized Ti_2CT_x/TiO_2 film, a different type of response was observed for the detection of almost all gases (except for NH_3 and NO_2, to which the maximum response was observed). When detecting CO, C_6H_6, C_3H_6O, C_2H_5OH, CH_4, H_2 and O_2, a *p*-type response was obtained, and when detecting nitrogen-containing gases NH_3 and NO_2 an *n*-type response was obtained.

Figure 8 shows the response of 4–100 ppm NH_3 and the signal reproducibility when detecting 10 ppm NH_3 by the Ti_2CT_x/TiO_2 composite film. As can be seen (Figure 8a), with an increase in NH_3 concentration from 4 to 100 ppm, there is a gradual increase in the response (S1) from 16% to 61% with a noticeable drift of the baseline (which can be explained by the high interaction energy of the ammonia molecule and receptor material), and the response itself is well reproduced (Figure 8b)

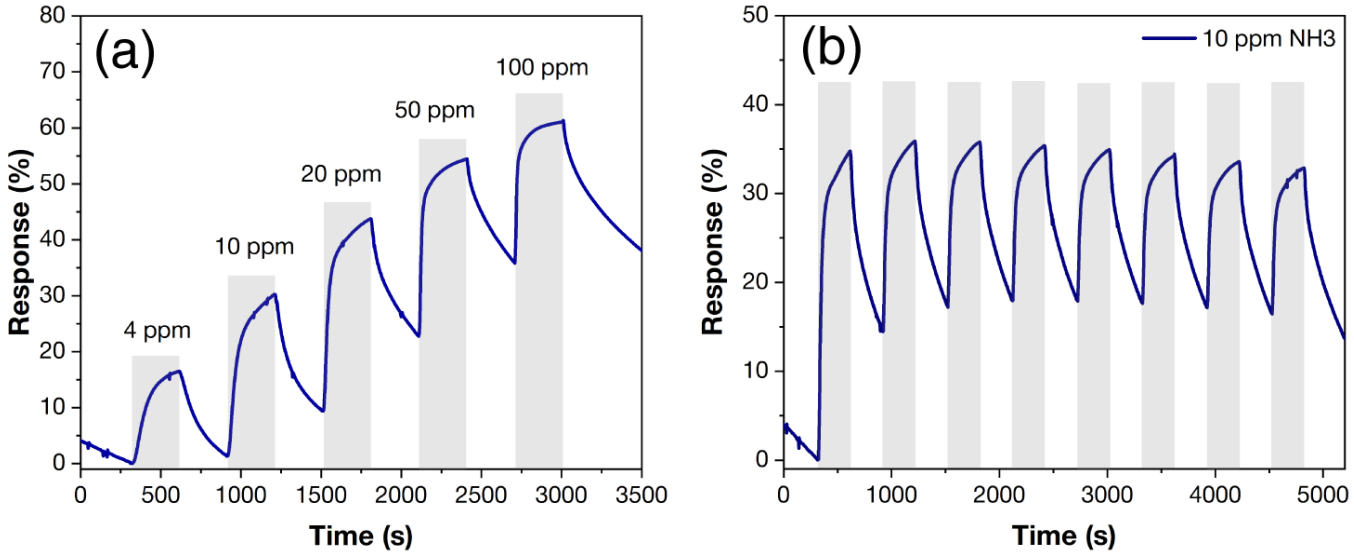

Figure 8. The gas-sensitive properties of the samples at RT and 50%RH. Responses of Ti_2CT_x/TiO_2 films to 4–100 ppm NH_3 (**a**) and 10 ppm NH_3 (**b**).

During the consideration of the mechanisms of the detection of various gases by the obtained materials, it is necessary to take into account the fact that all measurements were carried out in an atmosphere of 50% RH. Therefore, it can be assumed that the MXene surface, in this case, contains a large amount of sorbed water, as well as hydroxyl groups (OH^-), i.e., hydroxyl groups can be directly involved in reactions with various gases that precede the chemoresistive response.

In the present work, only the *n*-type response was observed for the initial Ti_2CT_x sample. When detecting the reducing gases (all gases in this work except NO_2 and O_2), this behavior is typical for *n*-type metal oxide semiconductors [52] but is not typical for $Ti_{n+1}C_nT_x$ MXenes, for which a *p*-type response is most often observed [15,18,53]. Raman spectroscopy and TEM data revealed that the surface of the initial MXene sheets contains oxygen groups, and an impurity of the rutile TiO_2 phase was noted. Thus, in addition to the hydroxyl functional groups of MXene, as well as sorbed water molecules, TiO_2 particles may also be involved in the detection mechanism. The presence of the *n*-type response detected in our study is not fully understood at this time and requires further investigation.

After oxidation of the initial MXene film in air to Ti_2CT_x/TiO_2 composite, a change in the response character from *n*- to *p*-type is observed when detecting CO, H_2 and VOC's. According to Raman spectroscopy data, it is found that a single *n*-type TiO_2 semiconductor phase is formed for this sample. The surface microstructure of the resulting composite also changes. As a rule, large-band-gap semiconductors, such as TiO_2, have poor electrical conductivity at room temperature. At room temperature, it is the MXene phase, which is characterized by *p*-type conductivity, that makes the main contribution to the gas sensitivity. The increase in sensing signals can be related to the fact that at the Ti_2CT_x/TiO_2 interface, a Schottky barrier appears, the height of which will change during the adsorption of different gases [23].

Table 1 provides information on the gas-sensitive properties of composites of MXenes $Ti_3C_2T_x/TiO_2$ and Ti_2CT_x/TiO_2 operating at room temperature for chemoresistive gas sensors reported in the literature. As can be seen, in the field of gas-sensing composites based on $Ti_3C_2T_x$, MXenes are mainly used, and the sensory properties of Ti_2CT_x MXenes and nanocomposite Ti_2CT_x/TiO_2 are practically not studied. For many of the composites presented in Table 1, it is ammonia that shows the greatest response. This corresponds to the data of theoretical calculations [54] for the maximum oxidized compound, Ti_2CO_2, which is associated with high adsorption energy and the calculated value of charge transfer. A comparison of the experimental data on the gas-sensitive properties shows that the materials obtained in this work have a sufficiently high response (to a wide range of NH_3 concentrations), significantly exceeding most of the literature analogs. The increased response can be attributed to the more flexible heat treatment conditions used in this work under the control of in situ Raman spectroscopy for the controlled formation of heterojunctions between Ti_2CT_x and TiO_2. In addition, the responses obtained in this work were recorded at relative humidity RH = 50% (closest to the real conditions), which has not been noted in other works for TiO_2-modified MXenes.

Table 1. Comparison of gas-sensitive characteristics of chemoresistive gas sensors based on $Ti_3C_2T_x/TiO_2$ and Ti_2CT_x/TiO_2 MXenes operating at room temperature that is presented in the literature.

No.	Year	Composition	Target Gas	Conc., ppm	Response	RH, %	Ref.
1	2019	$Ti_3C_2T_x/TiO_2$	NH_3	10 ppm	3%	60	[27]
2	2020	Ti_2CT_x/TiO_2	NH_3	10 ppm	1.9%	0	[25]
3	2020	$Ti_3C_2T_x/TiO_2$	NO_2	5 ppm	16.05%	0	[46]
4	2021	$Ti_3C_2T_x/TiO_2$	C_2H_5OH	100 ppm	22.47%	0	[55]
5	2021	$Ti_3C_2T_x/TiO_2$	hexanal	100 ppm	8.8%	0	[56]
6	2021	$Ti_3C_2T_x/TiO_2$	NO_2	100 ppm	4%	0	[26]
7	2021	$Ti_3C_2T_x$ (N-doped)/TiO_2	NH_3	200 ppb	7.3%	0	[57]
8	2022	$Ti_3C_2T_x/TiO_2$	C_2H_5OH	90 ppm	91 a.u.	0	[24]
9	2022	Ti_2CT_x/TiO_2	NH_3	4–100 ppm	16–61%	50	This work

4. Conclusions

The in situ oxidation of the film of layered Ti_2CT_x MXene synthesized as a result of the exposure of the MAX-phase of Ti_2AlC to sodium fluoride solution in hydrochloric acid, delaminated by tetramethylammonium hydroxide and held in water dispersion, has been studied, in detail, using Raman spectroscopy. The phenomenon of substrate (Al_2O_3 ceramics or platinum) influence on the intensity of Ti_2CT_x MXene phase modes, as well as the modes formed during oxidation in the air atmosphere of rutile and anatase phases, has been noted. It is shown that the formation of a new oxidation product phase (TiO_2 with anatase structure) on the ceramic Al_2O_3 substrate can be fixed at a lower temperature (316 °C) than it is typical for the Ti_2CT_x layer on the platinum electrodes of the specialized

substrate (372 °C). It was found that at 447 °C the full oxidation of the initial Ti_2CT_x MXene under the conditions of heating in an air atmosphere occurs.

The coating microstructure was studied using a complex of methods (SEM, TEM and AFM), and the work function was determined for both the Ti_2CT_x/TiO_2 composite obtained at 316 °C and the fully oxidized composition using Kelvin-probe force microscopy.

It was found that the obtained Ti_2CT_x and Ti_2CT_x/TiO_2 films exhibit chemoresistive responses when detecting a wide group of gases, H_2, CO, NH_3, C_6H_6, C_3H_6O, CH_4, C_2H_5OH and O_2, at room temperature and 50% relative humidity. It was shown that partial oxidation of MXene favors the gas-sensitive properties, and the most sensitivity was observed for NH_3.

Author Contributions: Conceptualization, A.S.M. and E.P.S.; Methodology, I.A.N. and E.P.S.; Validation, E.P.S.; Formal analysis, P.Y.G., A.A.A., T.L.S. and N.P.S.; Investigation, A.S.M.; Writing—original draft, A.S.M.; Writing—review & editing, E.P.S. and N.T.K.; Visualization, A.S.M.; Supervision, N.T.K.; Funding acquisition, N.P.S. All authors have read and agreed to the published version of the manuscript.

Funding: This work was supported by the Russian Science Foundation, project No. 21-73-10251, https://rscf.ru/en/project/21-73-10251/ (accessed on 29 November 2022).

Institutional Review Board Statement: Not applicable.

Informed Consent Statement: Not applicable.

Data Availability Statement: Not applicable.

Conflicts of Interest: The authors declare that they have no known competing financial interest or personal relationships that could have appeared to influence the work reported in this paper.

References

1. Naguib, M.; Mashtalir, O.; Carle, J.; Presser, V.; Lu, J.; Hultman, L.; Gogotsi, Y.; Barsoum, M.W. Two-Dimensional Transition Metal Carbides. *ACS Nano* **2012**, *6*, 1322–1331. [CrossRef] [PubMed]
2. Naguib, M.; Mochalin, V.N.; Barsoum, M.W.; Gogotsi, Y. 25th Anniversary Article: MXenes: A New Family of Two-Dimensional Materials. *Adv. Mater.* **2014**, *26*, 992–1005. [CrossRef] [PubMed]
3. Naguib, M.; Kurtoglu, M.; Presser, V.; Lu, J.; Niu, J.; Heon, M.; Hultman, L.; Gogotsi, Y.; Barsoum, M.W. Two-Dimensional Nanocrystals Produced by Exfoliation of Ti 3AlC 2. *Adv. Mater.* **2011**, *23*, 4248–4253. [CrossRef] [PubMed]
4. Kumar, K.S.; Choudhary, N.; Jung, Y.; Thomas, J. Recent Advances in Two-Dimensional Nanomaterials for Supercapacitor Electrode Applications. *ACS Energy Lett.* **2018**, *3*, 482–495. [CrossRef]
5. Aslam, M.K.; Xu, M. A Mini-Review: MXene Composites for Sodium/Potassium-Ion Batteries. *Nanoscale* **2020**, *12*, 15993–16007. [CrossRef]
6. Zhong, Y.; Xia, X.H.; Shi, F.; Zhan, J.Y.; Tu, J.P.; Fan, H.J. Transition Metal Carbides and Nitrides in Energy Storage and Conversion. *Adv. Sci.* **2016**, *3*, 1500286. [CrossRef]
7. Khan, K.; Tareen, A.K.; Aslam, M.; Zhang, Y.; Wang, R.; Ouyang, Z.; Gou, Z.; Zhang, H. Recent Advances in Two-Dimensional Materials and Their Nanocomposites in Sustainable Energy Conversion Applications. *Nanoscale* **2019**, *11*, 21622–21678. [CrossRef]
8. Li, K.; Zhang, S.; Li, Y.; Fan, J.; Lv, K. MXenes as Noble-Metal-Alternative Co-Catalysts in Photocatalysis. *Chin. J. Catal.* **2020**, *42*, 3–14. [CrossRef]
9. Xie, X.; Zhang, N. Positioning MXenes in the Photocatalysis Landscape: Competitiveness, Challenges, and Future Perspectives. *Adv. Funct. Mater.* **2020**, *30*, 2002528. [CrossRef]
10. Zhao, Q.; Zhou, W.; Zhang, M.; Wang, Y.; Duan, Z.; Tan, C.; Liu, B.; Ouyang, F.; Yuan, Z.; Tai, H.; et al. Edge-Enriched $Mo_2TiC_2T_x/MoS_2$ Heterostructure with Coupling Interface for Selective NO_2 Monitoring. *Adv. Funct. Mater.* **2022**, *32*, 2203528. [CrossRef]
11. Wang, H.; Shi, X.; Liu, F.; Duan, T.; Sun, B. Non-Invasive Rapid Detection of Lung Cancer Biomarker Toluene with a Cataluminescence Sensor Based on the Two-Dimensional Nanocomposite $Pt/Ti_3C_2T_x$-CNT. *Chemosensors* **2022**, *10*, 333. [CrossRef]
12. Choi, S.J.; Kim, I.D. Recent Developments in 2D Nanomaterials for Chemiresistive-Type Gas Sensors. *Electron. Mater. Lett.* **2018**, *14*, 221–260. [CrossRef]
13. Lee, E.; Kim, D.-J. Review—Recent Exploration of Two-Dimensional MXenes for Gas Sensing: From a Theoretical to an Experimental View. *J. Electrochem. Soc.* **2020**, *167*, 037515. [CrossRef]
14. Devaraj, M.; Rajendran, S.; Hoang, T.K.A.; Soto-Moscoso, M. A Review on MXene and Its Nanocomposites for the Detection of Toxic Inorganic Gases. *Chemosphere* **2022**, *302*, 134933. [CrossRef]

15. Kim, S.J.; Koh, H.J.; Ren, C.E.; Kwon, O.; Maleski, K.; Cho, S.Y.; Anasori, B.; Kim, C.K.; Choi, Y.K.; Kim, J.; et al. Metallic $Ti_3C_2T_x$ MXene Gas Sensors with Ultrahigh Signal-to-Noise Ratio. *ACS Nano* **2018**, *12*, 986–993. [CrossRef]
16. Ji, H.; Zeng, W.; Li, Y. Gas Sensing Mechanisms of Metal Oxide Semiconductors: A Focus Review. *Nanoscale* **2019**, *11*, 22664–22684. [CrossRef]
17. Khakbaz, P.; Moshayedi, M.; Hajian, S.; Soleimani, M.; Narakathu, B.B.; Bazuin, B.J.; Pourfath, M.; Atashbar, M.Z. Titanium Carbide MXene as NH_3 Sensor: Realistic First-Principles Study. *J. Phys. Chem. C* **2019**, *123*, 29794–29803. [CrossRef]
18. Majhi, S.M.; Ali, A.; Greish, Y.E.; El-Maghraby, H.F.; Qamhieh, N.N.; Hajamohideen, A.R.; Mahmoud, S.T. Accordion-like-Ti_3C_2 MXene-Based Gas Sensors with Sub-Ppm Level Detection of Acetone at Room Temperature. *ACS Appl. Electron. Mater.* **2022**, *4*, 4094–4103. [CrossRef]
19. Wang, J.; Xu, R.; Xia, Y.; Komarneni, S. Ti_2CT_x MXene: A Novel p-Type Sensing Material for Visible Light-Enhanced Room Temperature Methane Detection. *Ceram. Int.* **2021**, *47*, 34437–34442. [CrossRef]
20. Zhang, C.; Zhang, Y.; Cao, K.; Guo, Z.; Han, Y.; Hu, W.; Wu, Y.; She, Y.; He, Y. Ultrasensitive and Reversible Room-Temperature Resistive Humidity Sensor Based on Layered Two-Dimensional Titanium Carbide. *Ceram. Int.* **2021**, *47*, 6463–6469. [CrossRef]
21. Koh, H.J.; Kim, S.J.; Maleski, K.; Cho, S.Y.; Kim, Y.J.; Ahn, C.W.; Gogotsi, Y.; Jung, H.T. Enhanced Selectivity of MXene Gas Sensors through Metal Ion Intercalation: In Situ X-Ray Diffraction Study. *ACS Sens.* **2019**, *4*, 1365–1372. [CrossRef] [PubMed]
22. Wu, M.; An, Y.; Yang, R.; Tao, Z.; Xia, Q.; Hu, Q.; Li, M.; Chen, K.; Zhang, Z.; Huang, Q.; et al. V_2CT_x and $Ti_3C_2T_x$ MXenes Nanosheets for Gas Sensing. *ACS Appl. Nano Mater.* **2021**, *4*, 6257–6268. [CrossRef]
23. Pazniak, H.; Plugin, I.A.; Loes, M.J.; Inerbaev, T.M.; Burmistrov, I.N.; Gorshenkov, M.; Polcak, J.; Varezhnikov, A.S.; Sommer, M.; Kuznetsov, D.V.; et al. Partially Oxidized $Ti_3C_2T_x$ MXenes for Fast and Selective Detection of Organic Vapors at Part-per-Million Concentrations. *ACS Appl. Nano Mater.* **2020**, *3*, 3195–3204. [CrossRef]
24. Wang, Z.; Wang, F.; Hermawan, A.; Zhu, J.; Yin, S. Surface Engineering of $Ti_3C_2T_x$ MXene by Oxygen Plasma Irradiation as Room Temperature Ethanol Sensor. *Funct. Mater. Lett.* **2022**, *15*, 2251007. [CrossRef]
25. Sun, Q.; Wang, J.; Wang, X.; Dai, J.; Wang, X.; Fan, H.; Wang, Z.; Li, H.; Huang, X.; Huang, W. Treatment-Dependent Surface Chemistry and Gas Sensing Behavior of the Thinnest Member of Titanium Carbide MXenes. *Nanoscale* **2020**, *12*, 16987–16994. [CrossRef]
26. Liu, S.; Wang, M.; Liu, G.; Wan, N.; Ge, C.; Hussain, S.; Meng, H.; Wang, M.; Qiao, G. Enhanced NO_2 Gas-Sensing Performance of 2D Ti_3C_2/TiO_2 Nanocomposites by In-Situ Formation of Schottky Barrier. *Appl. Surf. Sci.* **2021**, *567*, 150747. [CrossRef]
27. Tai, H.; Duan, Z.; He, Z.; Li, X.; Xu, J.; Liu, B.; Jiang, Y. Enhanced Ammonia Response of $Ti_3C_2T_x$ Nanosheets Supported by TiO_2 Nanoparticles at Room Temperature. *Sens. Actuators B Chem.* **2019**, *298*, 126874. [CrossRef]
28. Simonenko, E.P.; Simonenko, N.P.; Nagornov, I.A.; Simonenko, T.L.; Mokrushin, A.S.; Sevastyanov, V.G.; Kuznetsov, N.T. Synthesis of MAX Phases in the Ti_2AlC-V_2AlC System as Precursors of Heterometallic MXenes $Ti_{2-X}V_xC$. *Russ. J. Inorg. Chem.* **2022**, *67*, 705–714. [CrossRef]
29. Simonenko, E.P.; Simonenko, N.P.; Nagornov, I.A.; Simonenko, T.L.; Gorobtsov, P.Y.; Mokrushin, A.S.; Kuznetsov, N.T. Synthesis and Chemoresistive Properties of Single-Layer MXene Ti_2CT_x. *Russ. J. Inorg. Chem.* **2022**, *67*, 1838–1847. [CrossRef]
30. Mokrushin, A.S.; Simonenko, T.L.; Simonenko, N.P.; Yu, P.; Bocharova, V.A.; Kozodaev, M.G.; Markeev, A.M.; Lizunova, A.A.; Volkov, I.A.; Simonenko, E.P.; et al. Microextrusion Printing of Gas-Sensitive Planar Anisotropic NiO Nanostructures and Their Surface Modification in an H_2S Atmosphere. *Appl. Surf. Sci.* **2022**, *578*, 151984. [CrossRef]
31. Mokrushin, A.S.; Nagornov, I.A.; Simonenko, T.L.; Simonenko, N.P.; Yu, P.; Khamova, T.V.; Kopitsa, G.P.; Evzrezov, A.N.; Simonenko, E.P.; Sevastyanov, V.G.; et al. Chemoresistive Gas-Sensitive ZnO/Pt Nanocomposites Films Applied by Microplotter Printing with Increased Sensitivity to Benzene and Hydrogen. *Mater. Sci. Eng. B* **2021**, *271*, 115233. [CrossRef]
32. Melchior, S.A.; Raju, K.; Ike, I.S.; Erasmus, R.M.; Kabongo, G.; Sigalas, I.; Iyuke, S.E.; Ozoemena, K.I. High-Voltage Symmetric Supercapacitor Based on 2D Titanium Carbide (MXene, Ti_2CT_x)/Carbon Nanosphere Composites in a Neutral Aqueous Electrolyte. *J. Electrochem. Soc.* **2018**, *165*, A501–A511. [CrossRef]
33. Habib, I.; Ferrer, P.; Ray, S.C.; Ozoemena, K.I. Interrogating the Impact of Onion-like Carbons on the Supercapacitive Properties of MXene (Ti_2CT_X). *J. Appl. Phys.* **2019**, *126*, 134301. [CrossRef]
34. Lioi, D.B.; Neher, G.; Heckler, J.E.; Back, T.; Mehmood, F.; Nepal, D.; Pachter, R.; Vaia, R.; Kennedy, W.J. Electron-Withdrawing Effect of Native Terminal Groups on the Lattice Structure of $Ti_3C_2T_x$ MXenes Studied by Resonance Raman Scattering: Implications for Embedding MXenes in Electronic Composites. *ACS Appl. Nano Mater.* **2019**, *2*, 6087–6091. [CrossRef]
35. Spanier, J.E.; Gupta, S.; Amer, M.; Barsoum, M.W. Vibrational Behavior of the $M_{n+1}AX_n$ Phases from First-Order Raman Scattering (M = Ti, V, Cr, A = Si, X = C, N). *Phys. Rev. B* **2005**, *71*, 012103. [CrossRef]
36. Ma, R.; Fukuda, K.; Sasaki, T.; Osada, M.; Bando, Y. Structural Features of Titanate Nanotubes/Nanobelts Revealed by Raman, X-Ray Absorption Fine Structure and Electron Diffraction Characterizations. *J. Phys. Chem. B* **2005**, *109*, 6210–6214. [CrossRef]
37. Ma, H.L.; Yang, J.Y.; Dai, Y.; Zhang, Y.B.; Lu, B.; Ma, G.H. Raman Study of Phase Transformation of TiO_2 Rutile Single Crystal Irradiated by Infrared Femtosecond Laser. *Appl. Surf. Sci.* **2007**, *253*, 7497–7500. [CrossRef]
38. Frank, O.; Zukalova, M.; Laskova, B.; Kürti, J.; Koltai, J.; Kavan, L. Raman Spectra of Titanium Dioxide (Anatase, Rutile) with Identified Oxygen Isotopes (16, 17, 18). *Phys. Chem. Chem. Phys.* **2012**, *14*, 14567–14572. [CrossRef]
39. Zhang, J.Z.; Shen, Y.D.; Li, Y.W.; Hu, Z.G.; Chu, J.H. Composition Dependence of Microstructure, Phonon Modes, and Optical Properties in Rutile TiO_2:Fe Nanocrystalline Films Prepared by a Nonhydrolytic Sol-Gel Route. *J. Phys. Chem. C* **2010**, *114*, 15157–15164. [CrossRef]

40. Gan, Y.; Zhu, F.; Shi, Y.; Wen, Q. Single Frequency Fiber Laser Base on MXene with KHz Linewidth. *J. Mater. Chem. C* **2021**, *9*, 2276–2281. [CrossRef]
41. Murugan, N.; Jerome, R.; Preethika, M.; Sundaramurthy, A.; Sundramoorthy, A.K. 2D-Titanium Carbide (MXene) Based Selective Electrochemical Sensor for Simultaneous Detection of Ascorbic Acid, Dopamine and Uric Acid. *J. Mater. Sci. Technol.* **2021**, *72*, 122–131. [CrossRef]
42. Liu, X.; Ji, L.; Zhu, F.; Gan, Y.; Wen, Q. Linear-Cavity-Based Single Frequency Fiber Laser with a Loop Mirror and Ti_2CT_x Quantum Dots. *Opt. Mater.* **2021**, *122*, 111686. [CrossRef]
43. Tan, Z.; Sato, K.; Ohara, S. Synthesis of Layered Nanostructured TiO_2 by Hydrothermal Method. *Adv. Powder Technol.* **2015**, *26*, 296–302. [CrossRef]
44. Waterland, M.R.; Stockwell, D.; Kelley, A.M. Symmetry Breaking Effects in NO^{3-}: Raman Spectra of Nitrate Salts and Ab Initio Resonance Raman Spectra of Nitrate-Water Complexes. *J. Chem. Phys.* **2001**, *114*, 6249–6258. [CrossRef]
45. Waterland, M.R.; Kelley, A.M. Far-Ultraviolet Resonance Raman Spectroscopy of Nitrate Ion in Solution. *J. Chem. Phys.* **2000**, *113*, 6760–6773. [CrossRef]
46. Choi, J.; Kim, Y.J.; Cho, S.Y.; Park, K.; Kang, H.; Kim, S.J.; Jung, H.T. In Situ Formation of Multiple Schottky Barriers in a Ti_3C_2 MXene Film and Its Application in Highly Sensitive Gas Sensors. *Adv. Funct. Mater.* **2020**, *30*, 2003998. [CrossRef]
47. Wang, Z.; Wang, F.; Hermawan, A.; Asakura, Y.; Hasegawa, T.; Kumagai, H.; Kato, H.; Kakihana, M.; Zhu, J.; Yin, S. SnO-SnO_2 Modified Two-Dimensional MXene $Ti_3C_2T_x$ for Acetone Gas Sensor Working at Room Temperature. *J. Mater. Sci. Technol.* **2021**, *73*, 128–138. [CrossRef]
48. Roy, A.; Sood, A.K. Phonons and Fractons in Sol-Gel Alumina: Raman Study. *Pramana* **1995**, *44*, 201–209. [CrossRef]
49. Xu, J.; Shim, J.; Park, J.H.; Lee, S. MXene Electrode for the Integration of WSe_2 and MoS_2 Field Effect Transistors. *Adv. Funct. Mater.* **2016**, *26*, 5328–5334. [CrossRef]
50. Khazaei, M.; Arai, M.; Sasaki, T.; Ranjbar, A.; Liang, Y.; Yunoki, S. OH-Terminated Two-Dimensional Transition Metal Carbides and Nitrides as Ultralow Work Function Materials. *Phys. Rev. B* **2015**, *92*, 075411. [CrossRef]
51. Mansfeldova, V.; Zlamalova, M.; Tarabkova, H.; Janda, P.; Vorokhta, M.; Piliai, L.; Kavan, L. Work Function of TiO_2 (Anatase, Rutile, and Brookite) Single Crystals: Effects of the Environment. *J. Phys. Chem. C* **2021**, *125*, 1902–1912. [CrossRef]
52. Deng, Y. Sensing mechanism and evaluation criteria of semiconducting metal oxides gas sensors. In *Semiconducting Metal Oxides for Gas Sensing*; Springer: Singapore, 2019; pp. 23–51. ISBN 9789811358524.
53. Lee, E.; Vahidmohammadi, A.; Prorok, B.C.; Yoon, Y.S.; Beidaghi, M.; Kim, D.J. Room Temperature Gas Sensing of Two-Dimensional Titanium Carbide (MXene). *ACS Appl. Mater. Interfaces* **2017**, *9*, 37184–37190. [CrossRef]
54. Yu, X.F.; Li, Y.C.; Cheng, J.B.; Liu, Z.B.; Li, Q.Z.; Li, W.Z.; Yang, X.; Xiao, B. Monolayer Ti_2CO_2: A Promising Candidate for NH_3 Sensor or Capturer with High Sensitivity and Selectivity. *ACS Appl. Mater. Interfaces* **2015**, *7*, 13707–13713. [CrossRef]
55. Hou, M.; Guo, S.; Yang, L.; Gao, J.; Hu, T.; Wang, X.; Li, Y. Improvement of Gas Sensing Property for Two-Dimensional $Ti_3C_2T_x$ Treated with Oxygen Plasma by Microwave Energy Excitation. *Ceram. Int.* **2021**, *47*, 7728–7737. [CrossRef]
56. Kuang, D.; Wang, L.; Guo, X.; She, Y.; Du, B.; Liang, C.; Qu, W.; Sun, X.; Wu, Z.; Hu, W.; et al. Facile Hydrothermal Synthesis of $Ti_3C_2T_x$-TiO_2 Nanocomposites for Gaseous Volatile Organic Compounds Detection at Room Temperature. *J. Hazard. Mater.* **2021**, *416*, 126171. [CrossRef]
57. Zhou, Y.; Wang, Y.; Wang, Y.; Yu, H.; Zhang, R.; Li, J.; Zang, Z.; Li, X. MXene $Ti_3C_2T_x$-Derived Nitrogen-Functionalized Heterophase TiO_2 Homojunctions for Room-Temperature Trace Ammonia Gas Sensing. *ACS Appl. Mater. Interfaces* **2021**, *13*, 56485–56497. [CrossRef]